Structural effects of Sc doping on the multiferroic TbMnO$_3$

Vera Cuartero,[1] Javier Blasco,[1,*] Joaquín García,[1] Gloria Subías,[1] Clemens Ritter,[2] and J. Alberto Rodríguez-Velamazán[1,2]

[1]*Instituto de Ciencia de Materiales de Aragón, Departamento de Física de la Materia Condensada, CSIC–Universidad de Zaragoza, C/Pedro Cerbuna 12, 50009 Zaragoza, Spain*

[2]*Institut Laue-Langevin, Boîte Postale 156, 38042 Grenoble Cèdex 9, France*

The new TbMn$_{1-x}$Sc$_x$O$_3$ series has been synthesized and the structural properties have been characterized by x-ray diffraction, neutron diffraction, and x-ray absorption spectroscopy. The whole series belongs to the family of ABO$_3$ perovskites. All of the samples are isostructural to the parent compound TbMnO$_3$, crystallizing in an orthorhombic cell with space-group *Pbnm* symmetry. The homovalent substitution of Mn^{3+} with the larger Sc^{3+} ion leads to an increase in both the unit-cell volume and the BO$_6$ octahedra tilting. The analysis of neutron and x-ray diffraction patterns suggest a continuous evolution from a Jahn-Teller distorted BO$_6$ octahedron in TbMnO$_3$ into a nearly regular one in TbScO$_3$. However, x-ray absorption measurements at the Mn K edge reveal that the local geometry around the Mn^{3+} cation remains distorted in the series even for high values of x. This result is in opposition to previous findings in similar compounds such as LaMn$_{1-x}$(Ga/Sc)$_x$O$_3$ and suggests that the strong orthorhombic distortion of the unit cell due to the small Tb^{3+} cation size favors the stability of the distorted MnO$_6$ octahedron in diluted systems. Long-range magnetic ordering is not found for $x \geq 0.3$ samples and there is not sign of ferromagnetism for $x=0.5$ in opposite to the behavior observed in the La-based compounds. Since Sc substitution induces a minor perturbation on the local structure of the Mn sublattice but magnetic ordering of both Mn and Tb sublattices disappear for a small degree of substitution, we conclude that the involved magnetic interactions should have a strong directional anisotropy and the Tb magnetic ordering strongly depends on the existence of a long-range coherent Mn ordering.

I. INTRODUCTION

Multiferroic materials are of great technological interest due to the coupling between magnetic and electric properties. This makes these materials very promising for industrial applications such as new devices in information storage.[1] Moreover, the multiferroics are also very striking from a fundamental point of view: the competing magnetic interactions which allow ferroelectricity (FE) are still a matter of study.[2–4] In this respect, the study of TbMnO$_3$ is of great current interest owing to the coexistence of magnetic ordering and ferroelectricity with a strong coupling between them.[5,6] At room temperature, TbMnO$_3$ is an orthorhombic distorted perovskite (ABO$_3$) described in the *Pbnm* (No. 62) space group.[7] The orthorhombic distortion is induced by cooperative tilts of the MnO$_6$ octahedra, which relief the structural strain produced by the small size of the Tb^{3+} cations.[8] Mn^{3+} with a $3d^4$ configuration is an active Jahn-Teller ion which reduces its energy by distorting its octahedral coordination by elongating or contracting two of the bonds to the ligands (tetragonal distortion) and then removing the degeneracy of e_g orbitals.

The simultaneous occurrence of magnetism and ferroelectricity is rare and the coupling between both properties is even more surprising. Focusing on perovskites with transition-metal oxides, magnetic interactions need unpaired $3d$ electrons whereas ferroelectricity is usually driven by hybridization of empty orbitals with occupied p orbitals of the coordinated oxygen ions.[9] TbMnO$_3$ is a peculiar magnetoelectric multiferroic showing antiferromagnetic ordering and FE below 27 K.[5] Mn^{3+} magnetic moments order at T_{Mn} =41 K while Tb^{3+} magnetic moments do so at T_{Tb}= 8 K.

The frustrated spiral spin order of Mn^{3+} in TbMnO$_3$ is thought to be at the origin of the appearing of FE.[6] However, the exact interplay between competing magnetic and electric interactions is not well understood so far. In order to shed light on this subject, both the finding of new multiferroics and the testing of the multiferroic robustness are important. With this in mind we have studied the effects of replacing Mn^{3+} by Sc^{3+} in the TbMnO$_3$ cell. TbScO$_3$ is isostructural to TbMnO$_3$ but possesses an almost regular BO$_6$ octahedron.[10] These scandates have been used as substrates in the epitaxial growth of BaTiO$_3$ thin films. The strain induced by this type of substrates produced an enhancement of FE.[11]

The substitution of Mn^{3+} by nonmagnetic ions should be detrimental to the magnetic ordering of the transition-metal sublattice. This is exactly what happens in hexagonal REMn$_{1-x}$Ga$_x$O$_3$ compounds with fivefold coordinated Mn atoms. However, this substitution also raises the ferrielectric Curie temperature.[12] In our case, the addition of the $3d^0$ ion Sc^{3+} should weaken the magnetic ordering of the metal transition sublattice but it could also favor the hybridization between empty metal-$3d$ orbitals and oxygen-$2p$ orbitals increasing thereby FE. At the same time this argumentation has to be approximate as it is known that this type of substitution leads to the formation of a ferromagnetic ground state for LaMn$_{1/2}$Ga$_{1/2}$O$_3$ and LaMn$_{1/2}$Sc$_{1/2}$O$_3$.[13,14] Therefore, the occurrence of new interplays between magnetic and electric degrees of freedom cannot be discarded along the TbMn$_{1-x}$Sc$_x$O$_3$ series. Previous attempts of studying the effects of diluting Mn^{3+} with nonmagnetic ions in TbMnO$_3$ were incomplete. The synthesis of TbMn$_{1-x}$Ga$_x$O$_3$ by conventional ceramic procedures just forms single phases up to $x \leq 0.4$.[15] The formation of competitive phases (garnet, Tb$_3$Ga$_5$O$_{12}$) made it impossible to

determine if ferromagnetism exists for $TbMn_{1/2}Ga_{1/2}O_3$ or not. It was, however, possible to realize that already for concentrations of $x \sim 0.1$ the substitution of Mn^{3+} by Ga^{3+} is very effective suppressing FE. This result may be an effect of adding a nonmagnetic cation with a full occupation of the $3d$ orbitals.

We have been successful in preparing the whole $TbMn_{1-x}Sc_xO_3$ series by solid-state methods. Its study will allow us to check the robustness of the magnetic interactions after diluting with a nonmagnetic ion. For this purpose, an accurate structural characterization is needed and we have carried it out combining different techniques. X-ray and neutron powder diffractions were used to determine the crystallographic structure and the long-range magnetic ordering whereas x-ray absorption spectroscopy at the Mn K and Tb L_3 edges was employed to follow the local structure of both atoms along the whole series. We have observed that the local structure around the Mn atoms remain unchanged in the whole series. This makes these compounds ideal to study the magnetic interactions existing in $TbMnO_3$ as the only change produced in the $TbMn_{1-x}Sc_xO_3$ compounds is the homovalent substitution of Mn^{3+} with a nonmagnetic cation. The surprising result is that only the little dilution effect induces a strong suppression of both magnetic orderings, Tb and Mn, well beyond what is expected for isotropic nearest-neighbor magnetic interactions.

II. EXPERIMENTAL SECTION

All the samples have been synthesized by ceramic methods. Stoichiometric amounts of Tb_4O_7, $MnCO_3$, and Sc_2O_3 were mixed and heated at 1000 °C for 12 h in air. The resulting powders were pressed into pellets and sintered at 1200 °C for 24 h also in air. The last step consisted on repressing and sintering the pellets at 1400 °C for 2 days in argon flow. We characterized the whole series (single phased) by x-ray powder diffraction and magnetic measurements. For neutron powder diffraction, 6 g. of $x=0.1, 0.3, 0.5, 0.7$, and 0.9 samples were prepared. Tiny impurities of MnO and Sc_2O_3 were detected in $x \geq 0.5$ samples which were taken into account in the structural refinement. The other two samples were single phases.

X-ray diffraction (XRD) patterns have been collected using a Rigaku D/max-B diffractometer with a copper rotating anode and a graphite monochromator in order to select the Cu K_α wavelength ($\lambda = 1.5418$ Å). The patterns were collected in a range $18° \leq 2\theta \leq 130°$ with a step $\Delta\theta = 0.03°$ at room temperature. The integration time was 5 s per point. Neutron-diffraction measurements were carried out on the high-resolution powder diffractometer D2B at the Institut Laue-Langevin (ILL) in Grenoble (France). The diffractograms were collected at selected temperatures ($T=300, 50, 30, 17, 10$, and 2 K) in an angular range $9° \leq 2\theta \leq 150°$ with $\Delta\theta = 0.05°$ using a wavelength of 1.59 Å. A neutron thermodiffractogram between 2 and 250 K was also measured for $TbMn_{1/2}Sc_{1/2}O_3$ using the high intensity D1B diffractometer with $\lambda \sim 2.52$ Å. The same setup was used to determine the modulation vector of $TbMn_{0.9}Sc_{0.1}O_3$. The software package program used for structural refinement was
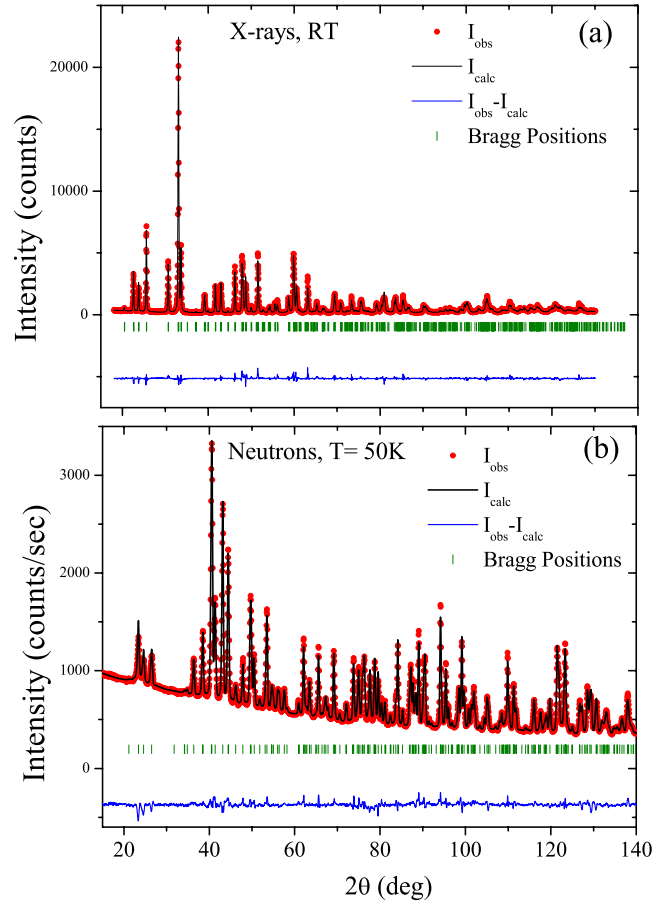

FIG. 1. (Color online) Rietveld refinements of $TbMn_{0.9}Sc_{0.1}O_3$ using (a) x-ray diffraction at room temperature and (b) neutron-diffraction pattern at 50 K.

FULLPROF.[16]

X-ray absorption spectroscopy measurements were performed at the European Synchrotron Radiation Facility (Grenoble, France), at the BM29 beamline[17] for measuring the Mn K edge and at BM25 for the Tb L_3 edge. In the first case, a double Si(111) crystal monochromator was used with an estimated energy resolution of $\Delta E/E \sim 10^{-4}$ and harmonic rejection better than 10^{-5} which was achieved using the Si coating of the double flat mirror installed after the monochromator. In the second case, a Si(111) pseudochannel-cut type monochromator was used and harmonic rejection was achieved by slightly detuning of the second crystal from the parallel arrangement. All spectra were collected at 50 K in transmission mode using ionization chambers as detectors. As reference samples, we used $TbMnO_3$ pellets for both edges. Extended x-ray absorption fine-structure (EXAFS) spectra were obtained after background subtraction and amplitude normalization using the Athena module (version 0.8.058) of IFEFFIT (version 1.2.11c) code.[18] The spectra were analyzed using theoretical amplitudes and phases calculated by FEFF 6.02 code.[19] The local structural analysis was made up to 3.3 Å in the case of Mn K edge and up to 4 Å in the case of Tb L_3 edge, both in the R-space fitting mode using the ARTEMIS (version 0.8.013) program.[18] The model used to fit the data includes Gaussian distributions for

TABLE I. Lattice parameters and mean interatomic distances at room temperature obtained from the refinement of x-ray diffraction patterns. Oxygen ions coordinates were fixed to the values obtained from the neutron-diffraction pattern refinement. Results for $TbScO_3$ are obtained from Ref. 10.

	$x=0.1$	$x=0.3$	$x=0.5$	$x=0.7$	$x=0.9$	$x=1$
a (Å)	5.3215(2)	5.3593(1)	5.3969(1)	5.4228(1)	5.4450(2)	5.4654(1)
b (Å)	5.8243(2)	5.7636(1)	5.7272(1)	5.7125(1)	5.7193(2)	5.7292(1)
c (Å)	7.4709(2)	7.6232(2)	7.7594(2)	7.8396(2)	7.8874(2)	7.9170(1)
B-O(1)	1.965(2)	2.017(2)	2.069(3)	2.082(2)	2.105(3)	2.109(3)
B-O(2)	2.213(1)	2.168(2)	2.163(2)	2.111(3)	2.104(2)	2.059(8)
B-O(2)	1.923(4)	1.968(2)	2.008(1)	2.047(3)	2.068(2)	2.088(7)
R_{Bragg} (%)	5.35	7.74	3.37	3.90	3.20	4.00
χ^2	5.02	4.18	2.33	2.80	1.84	1.84

the Mn-O, Mn-Tb, Tb-O, Tb-Mn, and Tb-Tb single-scattering paths. Debye-Waller factors and interatomic distances have been correlated through the Debye-temperature model.

III. RESULTS

$TbMn_{1-x}Sc_xO_3$ solid solutions can be prepared in the whole concentration range by conventional ceramic procedures. We have performed the structural refinement combining x-ray and neutron powder-diffraction techniques. The refinement of x-ray diffraction patterns allowed us to determine cell parameters with high precision. These parameters were utilized as starting point in the refinement of neutron-diffraction patterns. Conversely, neutron diffraction is more sensitive to the scattering of oxygen atoms so that the refined coordinates of these atoms obtained from the neutron pattern analysis were included and fixed in the last steps of the x-ray pattern refinements. Following this procedure, we have obtained reliable Tb-O and B-O (B =Mn, Sc) bond lengths and self-consistent results from both techniques. Figure 1 shows, as example, the fits obtained for $TbMn_{0.9}Sc_{0.1}O_3$ sample. The lattice parameters and selected bond lengths obtained from x-ray diffraction at room temperature are collected in Table I whereas Table II shows a

TABLE II. Structural parameters (lattice parameters, fractional coordinates, bond lengths, and bond angles) and reliability factors of the neutron powder-diffraction refinements at 50 K.

|	$x=0.1$	$x=0.3$	$x=0.5$	$x=0.7$	$x=0.9$
a (Å)	5.31643(8)	5.3486(2)	5.3806(2)	5.4047(1)	5.4345(2)
b (Å)	5.7844(1)	5.7362(2)	5.7005(2)	5.6878(2)	5.6947(2)
c (Å)	7.4387(1)	7.5893(3)	7.7267(2)	7.8052(3)	7.8646(3)
Tb: x	−0.0158(3)	−0.0175(5)	−0.0179(4)	−0.0206(6)	0.9817(5)
y	0.0766(2)	0.0712(4)	0.0666(3)	0.0651(4)	0.0603(3)
B (Å^2)	0.12(2)	0.22(4)	0.25(3)	0.27(4)	0.22(4)
Mn/Sc: B (Å^2)	0.84(7)	0.19(9)	0.45(4)	0.24(4)	0.11(3)
O1: x	0.1085(3)	0.1136(6)	0.1159(5)	0.1199(7)	0.1230(6)
y	0.4645(3)	0.4582(6)	0.4517(4)	0.4495(7)	0.4471(5)
B (Å^2)	0.30(3)	0.31(6)	0.61(4)	0.85(7)	0.38(5)
O2: x	0.7033(2)	0.6999(4)	0.6959(3)	0.6927(5)	0.6924(4)
y	0.3242(3)	0.3176(3)	0.3108(3)	0.3071(5)	0.3062(5)
z	0.0530(2)	0.0569(3)	0.0603(2)	0.0619(3)	0.0631(3)
B (Å^2)	0.29(2)	0.45(3)	0.64(3)	0.88(4)	0.50(3)
B-O1	1.9579(5)	2.0081(5)	2.0479(9)	2.076(1)	2.098(1)
B-O2	2.200(1)	2.158(1)	2.114(2)	2.090(3)	2.093(3)
B-O2	1.918(1)	1.963(2)	2.014(2)	2.048(3)	2.064(2)
$\langle B$-O(1)-$B\rangle$	143.55(2)	141.76(2)	141.12(4)	140.05(5)	138.10(4)
$\langle B$-O(2)-$B\rangle$	145.02(4)	144.12(4)	143.41(8)	142.8(1)	142.5(1)
R_{Bragg} (%)	4.60	5.46	4.46	7.46	4.73
$R_{wp}\|R_F$	9.27‖2.96	11.9‖2.98	9.47‖2.72	13.6‖4.28	9.90‖2.80
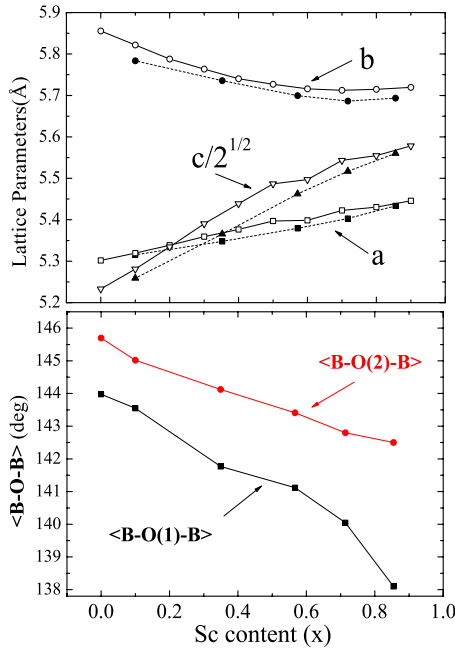
FIG. 2. (Color online) Upper panel: evolution of the lattice parameters with the composition at room temperature (open symbols) and at 50 K (black symbols). Lower panel: evolution of the $\langle B\text{-}O\text{-}B \rangle$ bond angles along the series at 50 K.

full set of refined structural parameters at 50 K obtained from the neutron experiments.

According to the lattice parameters, it is possible to distinguish between two orthorhombic phases. For the Mn-rich region ($x \leq 0.2$), we find that $c/\sqrt{2} \leq a < b$ while $a < c/\sqrt{2} < b$ for the rest of the samples. Along the whole series, b decreases up to $x \leq 0.7$, staying then almost constant, whereas a and c increase in value uniformly with increasing Sc content. These trends can be visualized in Fig. 2. The net effect is an increase in the unit-cell volume as the Sc concentration does. This result is expected due to the larger Sc^{3+} ionic size (0.745 Å) with respect to Mn^{3+} (0.645 Å).[20] Considering the bond lengths, Tables I and II show how the B-O distances get closer as the percentage of Jahn-Teller ions decreases becoming almost equal for $x=0.9$. Similar results were found in the $LaMn_{1-x}Ga_xO_3$ and $LaMn_{1-x}Sc_xO_3$ compounds although the equivalence in the bond lengths was achieved around $x=0.6$ in these cases.[13,14] Therefore, the BO_6 octahedron becomes more regular with increasing the Sc^{3+} content but it becomes as well bigger and consequently there is more left space for Tb^{3+} cations when diluting with Sc. This fact leads to a decrease in the B-O-B bond angles (an increase in the tilting of anion octahedra) in order to release strains. This result can be appreciated in the lower panel of Fig. 2.

The existence of long-range magnetic ordering was tested by neutron powder diffraction. Figure 3(a) compares the patterns obtained for $TbMn_{0.9}Sc_{0.1}O_3$ at different temperatures. The diagram obtained at 30 K shows the first magnetic superlattice peak ascribed to the long-range magnetic ordering of Mn^{3+} ions. The magnetic contribution can be refined in a sine-wave magnetic structure propagating along the b axis, similar to the one reported for the parent compound $TbMnO_3$.[7,21,22] We obtain a propagation vector $\mathbf{k}_{Mn}=(0, q_b \sim 0.26, 0)$ at 30 K. The temperature dependence of this vector is shown in Fig. 3(b). Its modulus decreases continuously on cooling down to ~ 25 K and it remains almost constant and very close to the commensurate value ($q_b \sim 0.25$) below this temperature. This change in slope is typical for the lock-in transition ascribed to the development of FE.[5,23] The refined magnetic moment is $2.55(5)\mu_B$ at 10 K. Comparing these values to the ones reported for $TbMnO_3$, we observe a decrease in both the amplitude and the propagation vector of the magnetic modulation. Both features might be related to the incorporation of Sc^{3+} into the Mn sublattice, reflecting a change in the strength of the competitive magnetic interactions. Below 10 K, the magnetic contribution from Tb^{3+} ions appears as a broad bump indicating a short-range magnetic ordering.

The rest of the samples do not show magnetic scattering on decreasing temperature indicating the lack of long-range magnetic orderings in both sublattices. This result reveals that this type of Sc dilution is strongly detrimental for the magnetic ordering developed in $TbMnO_3$. In related systems with other magnetic structures, the Mn long-range ordering is preserved up to dilutions of $x > 0.3$.[24] In the particular case of $LaMn_{1-x}Ga_xO_3$, the Mn dilution produces a canting of the A-magnetic structure which evolves into a ferromagnetic ground state at $x \sim 0.5$.[13] In order to ensure the lack of fer-
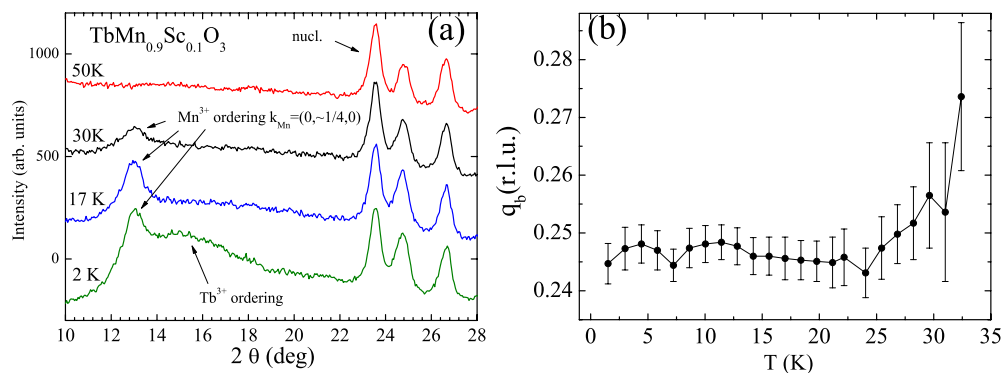

FIG. 3. (Color online) (a) Neutron-diffraction patterns for $TbMn_{0.9}Sc_{0.1}O_3$ at selected temperatures. Magnetic and nuclear contributions are indicated by arrows. (b) Temperature evolution of the propagating vector $\mathbf{k}_{Mn}=(0, q_b, 0)$ for $TbMn_{0.9}Sc_{0.1}O_3$. The data were collected on heating.
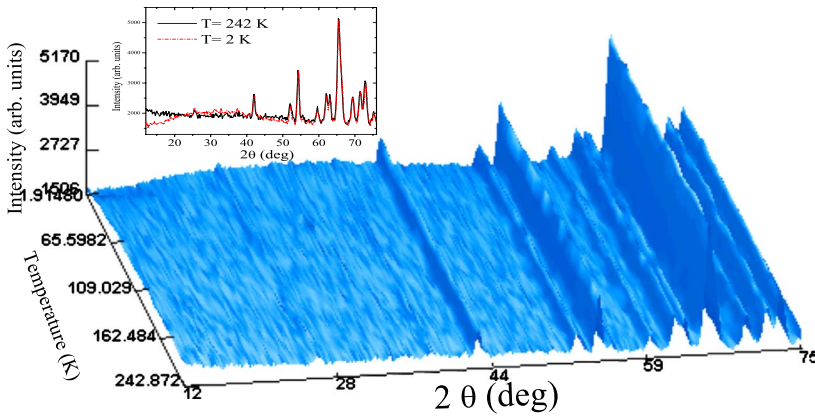
FIG. 4. (Color online) Neutron thermodiffractogram for $TbMn_{0.5}Sc_{0.5}O_3$ between 242 and 2 K. Inset: comparison between the patterns taken at 242 and 2 K.

romagnetism in $TbMn_{1/2}Sc_{1/2}O_3$, thermodiffractograms were collected on D1B at the ILL. The absence of any kind of magnetic ordering is demonstrated in Fig. 4.

The evolution of the Mn local structure after dilution was probed by measuring EXAFS spectra at the Mn K edge at 50 K for the whole series. Figure 5 shows the Fourier transform (FT) of the k-weighted EXAFS signal calculated between 3 and 12 Å using a sine window. The inset displays a typical EXAFS signal analyzed. The modulus of the FT spectra of all samples shows a main peak at ∼1.4 Å corresponding to the first (Mn-O) coordination shell without phase-shift correction. The intensity and shape of this peak is practically independent of the dilution indicating that the oxygen coordination geometry around Mn remains almost constant for the whole series. The contribution from further shells, Mn-Tb, Mn-Mn(Sc), and Mn-O, gives rise to a set of weak and broad peaks between 1.8 and 2.8 Å. Their low intensities suggest a large number of different paths with destructive interferences. This fact is in agreement with the high orthorhombic distortion of their crystallographic structures.

Fits for selected compounds are also displayed in Fig. 5(b). In these fits, the starting point for all samples was the crystallographic data of $TbMnO_3$ at 50 K. The coordination numbers were fixed to their crystallographic values and the

amplitude reduction factor s_0^2 was fixed to 0.84 for all samples. Therefore, only bond lengths, Debye-Waller (σ^2) factors, and the threshold energy were refined. The results of these fits for the first coordination shell are summarized in Table III. The fit was performed with three different Mn-O distances following the crystallographic structure but we have to recall here that EXAFS sensitivity is not able to distinguish between the two shortest distances. In agreement with the lack of changes observed in the first peak of Fig. 5, all samples show the same distribution of Mn-O distances composed by two short pairs and one long pair of Mn-O bond lengths. The short distances slightly increase with dilution but the octahedral distortion itself remains for all x value. We have tested the possibility of fitting the spectra using a single Mn-O distance (regular octahedron) with large values of σ^2 but the refinements were clearly worse. This result implies that the MnO_6 octahedron remains distorted along the whole series. Since the BO_6 distortion diminishes with increasing dilution of Mn^{3+} cations, as shown by diffraction refinements, the solid solutions would be composed by distorted MnO_6 and regular ScO_6 octahedra randomly distributed. In order to verify this point, we have carried out two tests. First, we have compared the refined B-O distances obtained from neutron diffraction with the weighted sum of the
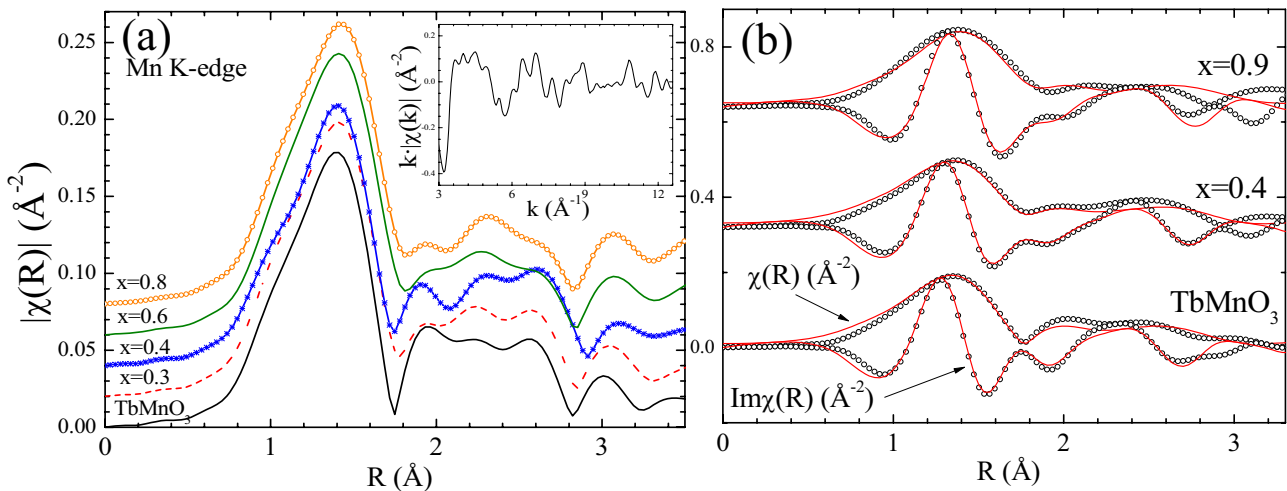

FIG. 5. (Color online) Left graph: Fourier transform of the experimental $k\chi(k)$ signals at the Mn K edge. Inset: EXAFS spectra (k weighted) at the Mn K edge of $TbMnO_3$ sample. Right graph: modulus and imaginary part of the experimental Fourier transforms (symbols) together with its fit (red lines) for samples $x=0$, 0.4, and 0.9 at the Mn K edge.

TABLE III. Fit results for Mn-O distances (Å), from structural analysis of the first and second coordination shells at the Mn K edge. σ^2 represent Debye-Waller factor (Å^2). $S_0^2=0.84$ and E_0 ranges from -3.1 to -1.1 eV (±1.7 eV).

	O$\times$2	$\sigma^2\times10^{-3}$	O$\times$2	$\sigma^2\times10^{-3}$	O$\times$2	$\sigma^2\times10^{-3}$	R_{factor}
$x=0$	1.90(2)	4.3	1.93(2)	4.3	2.22(4)	4.8	0.034
$x=0.1$	1.90(2)	3.7	1.93(2)	3.7	2.22(3)	4.1	0.041
$x=0.3$	1.91(2)	4.6	1.94(2)	4.6	2.20(5)	5.1	0.048
$x=0.4$	1.92(2)	5.5	1.95(2)	5.6	2.21(4)	6.2	0.043
$x=0.6$	1.92(3)	4.1	1.95(3)	4.1	2.19(6)	4.6	0.066
$x=0.8$	1.95(2)	4.7	1.98(2)	4.7	2.23(3)	5.3	0.092
$x=0.9$	1.96(2)	3.7	1.99(2)	3.7	2.24(3)	4.2	0.079

Mn-O distances determined by EXAFS and the Sc-O distances taken from in TbScO$_3$.[10] As it is shown in Fig. 6, the agreement between the averaged B-O distances and this sum is very good. The precise agreement between model and data also indicates that the geometrical orientation of the MnO$_6$ distortion is conserved in the *ab* plane along the whole series. Second, we have refined the XRD patterns using a model where the oxygen atoms are randomly distributed between two sites (corresponding to the oxygen coordinates obtained in the refinements of TbMnO$_3$ and TbScO$_3$, respectively) with the statistical occupation given by the composition. The quality of the fit was similar to the model using a single set of oxygen coordinates for each oxygen position. Therefore, both tests support a solid solution formed by a random distribution of distorted MnO$_6$ and undistorted ScO$_6$ octahedra.

The existence of MnO$_6$ octahedra with a tetragonal distortion in a diluted system is a new and surprising result. Previous findings in LaMn$_{1-x}$Ga$_x$O$_3$ revealed that the Jahn-Teller distorted MnO$_6$ octahedron transforms into a regular octahedron with dilution and this transformation is nearly coinciding with the appearance of long-range
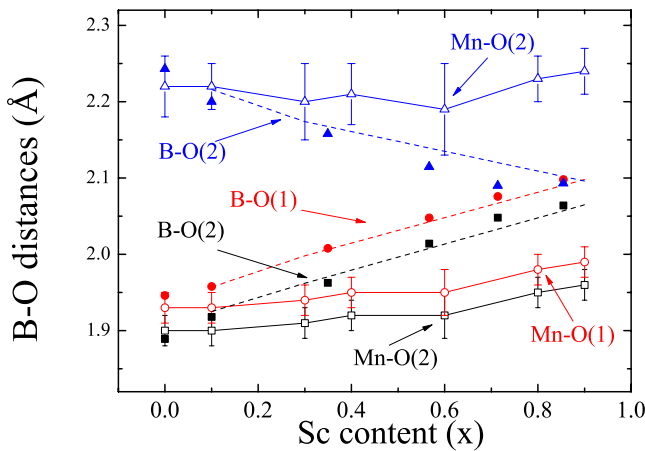

FIG. 6. (Color online) Evolution of Mn-O distances along the series (open symbols) obtained from EXAFS analysis. The *B*-O distances calculated by weighted average of the previous Mn-O distances and Sc-O distances (dotted line) are compared to the experimental *B*-O bond lengths obtained from neutron-diffraction refinements (closed symbols).
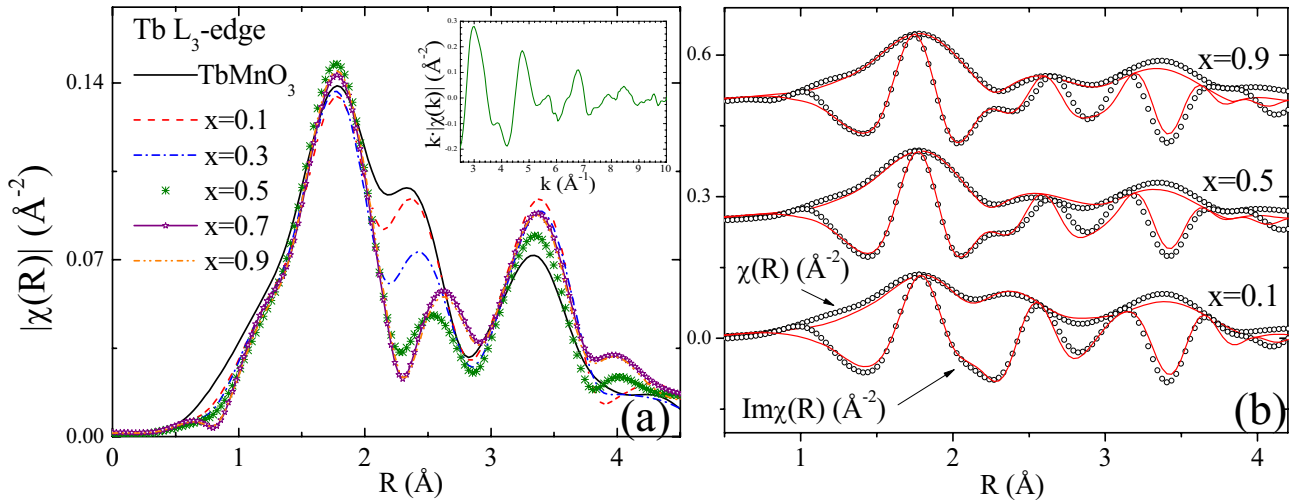
ferromagnetism.[25] The overall reduction in such a distortion in the MnO$_6$ octahedron was explained by an orbital-flipping model[26] whereas the occurrence of ferromagnetism has been recently ascribed to the orbital mixing of Mn orbitals due to the structural bias effect of the orthorhombic cell with *Pbnm* symmetry.[27] The instability of isolated distorted MnO$_6$ octahedra was confirmed in a study of LaB_{1-x}Mn$_x$O$_3$ samples (B=Ga or Sc) with a very diluted Mn^{3+} concentration. This suggested that the Mn clusters have to have a minimum size in order to show the tetragonal distortion typical of Jahn-Teller Mn^{3+} ions.[28] The persistence of this type of distortion in the whole TbMn$_{1-x}$Sc$_x$O$_3$ series adds a new factor not previously considered, the degree of the anion octahedra tilting. This is the main difference between the TbMn$_{1-x}$Sc$_x$O$_3$ and the LaMn$_{1-x}$Ga$_x$O$_3$ series. While the *B*-O-*B* bond angle exhibits values of around 160° in the second series,[14] it stays below 145° in the first one. The shrink of this angle weakens the superexchange magnetic interactions[29] and the orbital mixing[27] and consequently, a different magnetic behavior is obtained. In this case, the formation of a regular MnO$_6$ octahedron is destabilized remaining with the tetragonal distortion and this structural change might be related to the lack of long-range ferromagnetic ordering for $x\sim0.5$.

In order to complete the structural analysis, the local structure of the Tb^{3+} cations has been probed by measuring the EXAFS spectra at the Tb L_3 edge. The inset of Fig. 7(a) shows a typical k-weighted EXAFS signal extracted as explained in the experimental section. The FT spectra of these signals between 3 and 10 Å using a sine window (without phase-shift correction) are also displayed in Fig. 7(a). They show two peaks between 1 and 3 Å corresponding to the first coordination shell composed of several Tb-O distances. Further coordination shells [Tb-O, Tb-Mn(Sc), and Tb-Tb] contribute to a third peak located at around 3.4 Å. The main change in these spectra with increasing dilution concerns the intensity and position of the second peak. This peak is shifted to the right and its size decreases as the Sc content in the sample increases. This fact is related to changes in the first coordination shell of the Tb^{3+} cations. In an ideal cubic perovskite, Tb would be 12-fold coordinated to oxygen atoms with a single distance. Its small size leads to the tilting of BO$_6$ octahedra approaching some oxygen atoms and moving away from others. In practice, Tb is coordinated to eight oxygen atoms at distances below 2.8 Å while the other four atoms are at distances well above 3 Å. The EXAFS analysis

FIG. 7. (Color online) Left graph: Fourier transform of the experimental $k\chi(k)$ signals at the Tb L_3 edge. Inset: EXAFS spectra (k weighted) at the Tb L_3 edge of TbMn$_{0.9}$Sc$_{0.1}$O$_3$ sample. Right graph: modulus and imaginary part of the experimental Fourier transforms (black holes) together with its fit (red lines) for samples $x=0.1$, 0.5, and 0.9 at the Tb L_3 edge.

will allow us to monitor the changes in these bond lengths.

The structural analysis was carried out between 1.2 and 4 Å in the R-space fitting mode and selected fits are shown in Fig. 7(b). The fitting procedure employed was similar to the one previously reported for data taken at the Mn K edge. We have used the crystallographic data as starting model for the fits. The structural parameters obtained for the first coordination shell are collected in Table IV. We note here that EXAFS cannot discriminate between the shorter Tb-O distances as differences are smaller than 0.1 Å but we have maintained the crystallographic distribution. Figure 8 shows the evolution of the Tb-O distances below 3 Å along the whole series. Panels (a) and (b) correspond to the data obtained from EXAFS and neutron powder-diffraction refinements, respectively. The agreement between the results of the two techniques is very nice. Both indicate that the dilution does not affect the shorter Tb-O distances. However, the longer Tb-O distance at 2.66 Å increases with dilution up to 2.79 Å for $x=0.5$ before becoming almost constant (see Fig. 8). The destructive interference with the other long Tb-O distance ($\sim$2.55 Å) increases giving rise to the decrease in the intensity of the second peak in the FT spectra shown in Fig. 7(a). The expansion of the longer Tb-O bond length is related to the increase in the BO_6 rotation in agreement with the previous analysis.

IV. DISCUSSION AND CONCLUSIONS

The series of TbMn$_{1-x}$Sc$_x$O$_3$ compounds can be prepared by solid-state reaction for any value of x. The crystallographic structure remains orthorhombic, *Pbnm*, for the whole series. The homovalent substitution of Mn^{3+} by Sc^{3+} induces a small and monotonous variation in the lattice parameters leading to an increase in the volume of the cell, as expected due to the larger ionic radius of the Sc atom.[20] Simultaneously, the averaged tilting of the BO_6 octahedra slightly increases as the substitution progresses. Powder-diffraction refinements show that the tetragonal distortion of the BO_6 octahedron decreases with increasing the Sc content giving rise to a nearly regular BO_6 octahedron for $x=0.9$. On the other hand, EXAFS at the Mn K edge have shown that the MnO$_6$ octahedron remains tetragonal distorted as in TbMnO$_3$ even for the largest Sc substitution revealing the strong stability of this type of distortion in this system. Both pieces of structural information are complementary and provide us a realistic description of TbMn$_{1-x}$Sc$_x$O$_3$ samples. They are composed by a random distribution of regular ScO$_6$ and distorted MnO$_6$ octahedra. Moreover the longest Mn-O distance is always in the ab plane as deduced from the comparison of Fig. 6. Therefore, the Sc substitution produces a minimum disturbance on the local structural and electronic

TABLE IV. Fit results for Tb-O distances (Å) from structural analysis of the first and second coordination shells at the Tb L_3 edge. σ^2 represent Debye-Waller factor (Å^2). $S_0^2 = 1$ and E_0 ranges from 5.8 to 3.5 eV (± 2.7 eV).

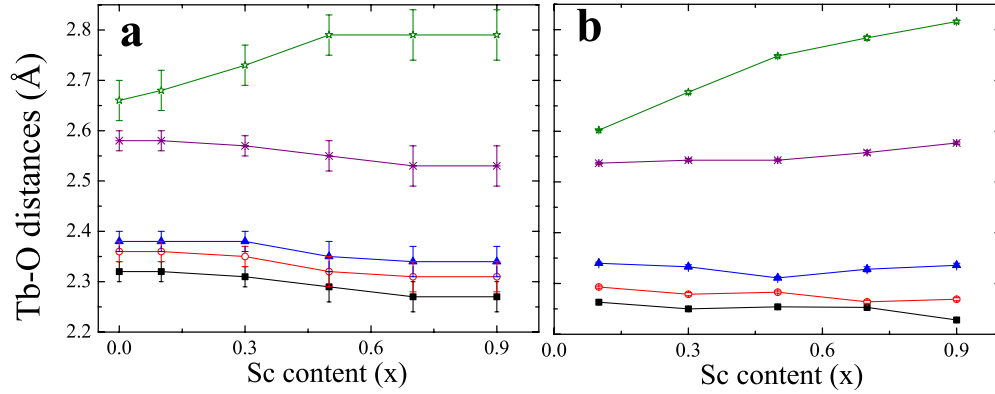|	O×1	$\sigma^2 \times 10^{-3}$	O×1	$\sigma^2 \times 10^{-3}$	O×2	$\sigma^2 \times 10^{-3}$	O×2	$\sigma^2 \times 10^{-3}$	O×1	$\sigma^2 \times 10^{-3}$	R_{factor}
$x=0$	2.32(2)	4.3	2.36(2)	4.3	2.38(2)	4.3	2.58(2)	4.5	2.66(4)	4.5	0.04
$x=0.1$	2.32(2)	4.7	2.36(2)	4.6	2.38(2)	4.7	2.58(2)	4.7	2.68(4)	4.8	0.04
$x=0.3$	2.31(2)	4.2	2.35(2)	4.2	2.38(2)	4.3	2.57(2)	4.4	2.73(4)	4.4	0.06
$x=0.5$	2.29(3)	3.0	2.32(3)	3.0	2.35(3)	3.0	2.55(3)	3.1	2.79(4)	3.2	0.07
$x=0.7$	2.27(3)	4.0	2.31(3)	4.0	2.34(3)	4.0	2.53(3)	4.1	2.79(5)	4.2	0.10
$x=0.9$	2.27(3)	3.7	2.31(3)	3.7	2.34(3)	3.7	2.53(3)	3.9	2.79(5)	3.9	0.10

FIG. 8. (Color online) Left graph: evolution of Tb-O distances along the series, resulting from the analysis of Tb L_3 edge EXAFS. Right graph: the same evolution but obtained from neutron-diffraction data refinement.

properties of the Mn sublattice. First, the valence state of the Mn atoms remains unchanged (3+). Second, the octahedron shows the same distortion and finally, this distortion conserves its orientation in the lattice. This behavior contrasts with the one observed in the $LaMn_{1-x}Ga_xO_3$ series, where the tetragonal distortion of the MnO_6 octahedron decreases with the Ga substitution[25,28] and the appearing of ferromagnetism concurs with the presence of regular MnO_6 octahedra. The stability of the tetragonal distorted MnO_6 octahedron in $TbMn_{1-x}Sc_xO_3$ prevents the formation of a ferromagnetic ground state for $x=0.5$ and suggests a close relationship between local structure around Mn^{3+} and the magnetic behavior in the diluted samples.

Despite the minimum local structural effect after dilution with Sc, the magnetic ordering of $TbMnO_3$ is strongly affected. First, the ordered Mn^{3+} magnetic-moment value decreases for $x=0.1$ and the propagation vector of the modulated magnetic structure tends to the commensurate value of $\mathbf{k}_{Mn}=(0, \sim \frac{1}{4}, 0)$. For higher Sc contents ($x \geq 0.3$), there is no longer long-range Mn magnetic ordering. Second, the long-range Tb magnetic ordering also disappears, reflecting the strong coupling of this ordering with that of the Mn sublattice. Similar conclusions have been recently obtained by Ga doping on $TbMnO_3$.[15,23] As it is well known, incommensurate magnetic ordering and its coupled ferroelectricity in $TbMnO_3$ have been essentially explained in a nearest-neighbor interaction model as a result of the competition between the different exchange interactions (J_{Mn-Mn}, J_{Mn-Tb}, and J_{Tb-Tb}) including the Dzyaloshinsky-Moriya (D_{Mn-Mn}) mechanism.[30] In this model, the effect of very little Sc dilution ($x \geq 0.1$) should follow the percolation theory giving rise to a continuous and less dramatic effect on the magnetic order instead of the strong suppression of both Tb and Mn magnetic orderings. We recall here that the percolation limit is found for an occupation fraction of magnetic ions (p) depending on the system dimensionality and the number of interactions. In the case of a simple-cubic perovskite lattice

with isotropic nearest-neighbor interactions, this limit is $p=0.31$.[31] This implies that we observe the loss of long-range magnetic ordering for compositions ($x=0.3$) with a concentration of magnetic ions two times higher than the percolation limit. We note here that $TbMnO_3$ is not an isotropic simple perovskite but a frustrated system. Even in this case, the effect of little dilution can modify the magnetic interactions but not lead to a complete suppression of the magnetic orderings. This drastic suppression can be understood if the nearest-neighbor magnetic interactions have a low dimensionality character. In this way, p is around 0.59 and 1 for a quadratic two-dimensional lattice[32] and a linear chain, respectively. Moreover, the strong magnetic anisotropy observed[21] in $TbMnO_3$ (Ref. 21) supports a directional anisotropy of these magnetic interactions.

Summarizing, substitution of Mn by Sc in the $TbMnO_3$ lattice does not significantly modify the MnO_6 octahedron and this series is the ideal example to study the effects of magnetic dilution. The strong changes in the magnetic properties with a few dilution indicates that long-range magnetic ordering is very sensitive to impurities and a long-range coherent composition is needed to develop the incommensurate magnetic ordering. Therefore, magnetic interactions in $TbMnO_3$ must present a strong low-dimensional anisotropy and there is also a significant coupling between Mn and Tb magnetic orderings.

*Corresponding author. FAX: +34-976-761229; jbc@posta.unizar.es

[1] N. Spaldin and M. Fiebig, Science **309**, 391 (2005).

[2] N. A. Hill, J. Phys. Chem. B **104**, 6694 (2000).

[3] C. N. R. Rao and C. R. Serrao, J. Mater. Chem. **17**, 4931 (2007).

[4] T. A. Tyson, T. Wu, K. H. Ahn, S. B. Kim, and S. W. Cheong, Phys. Rev. B **81**, 054101 (2010).

[5] K. Kimura, T. Goto, H. Shintani, K. Ishizka, T. Arima, and Y. Tokura, Nature (London) **426**, 55 (2003).

[6] S.-W. Cheong and M. Mostovoy, Nature Mater. **6**, 13 (2007).

[7] J. Blasco, C. Ritter, J. García, J. M. de Teresa, J. Pérez-Cacho, and M. R. Ibarra, Phys. Rev. B **62**, 5609 (2000).

[8] A. M. Glazer, Acta Crystallogr., Sect. A: Cryst. Phys., Diffr., Theor. Gen. Crystallogr. **31**, 756 (1975).

[9] R. E. Cohen, Nature (London) **358**, 136 (1992).

[10] R. P. Liferovich and R. H. Mitchell, J. Solid State Chem. **177**, 2188 (2004).

[11] K. J. Choi, M. Biegalski, Y. L. Li, A. Sharan, J. Schubert, R. Uecker, P. Reiche, Y. B. Chen, X. Q. Pan, V. Gopalan, L.-Q. Chen, D. G. Schlom, and C. B. Eom, Science **306**, 1005 (2004).

[12] H. D. Zhou, J. C. Denyszyn, and J. B. Goodenough, Phys. Rev. B **72**, 224401 (2005).

[13] J. B. Goodenough, R. I. Dass, and J. S. Zhou, Solid State Sci. **4**, 297 (2002).

[14] J. Blasco, J. García, J. Campo, M. C. Sánchez, and G. Subías, Phys. Rev. B **66**, 174431 (2002).

[15] V. Cuartero, J. Blasco, J. García, G. Subías, and M. C. Sánchez, J. Phys.: Conf. Ser. **200**, 012024 (2010).

[16] J. Rodríguez-Carvajal, Physica B **192**, 55 (1993); http://www.ill.eu/sites/fullprof/

[17] A. Filipponi, M. Borowski, D. T. Bowron, S. Ansell, A. Di Cicco, S. De Panfilis, and J. P. Itie, Rev. Sci. Instrum. **71**, 2422 (2000).

[18] M. Newville, J. Synchrotron Radiat. **8**, 322 (2001); B. Ravel and M. Newville, *ibid.* **12**, 537 (2005).

[19] J. J. Rehr and R. C. Albers, Rev. Mod. Phys. **72**, 621 (2000); see also http://leonardo.phys.washington.edu/feff/

[20] R. D. Shannon, Acta Crystallogr., Sect. A: Cryst. Phys., Diffr., Theor. Gen. Crystallogr. **32**, 751 (1976).

[21] S. Quezel, F. Tcheou, J. Rossat-Mignod, G. Quezel, and E. Roudaut, Physica B & C **86-88**, 916 (1977).

[22] R. Kajimoto, H. Yoshizawa, H. Shintani, T. Kimura, and Y. Tokura, Phys. Rev. B **70**, 012401 (2004).

[23] O. Prokhnenko, N. Aliouane, R. Feyerherm, E. Dudzik, A. U. B. Wolter, A. Maljuk, K. Kiefer, and D. N. Argyriou, Phys. Rev. B **81**, 024419 (2010).

[24] S. Malo, A. Maignan, M. Hervieu, K. R. Poeppelmeier, and B. Raveau, Solid State Sci. **7**, 1492 (2005).

[25] M. C. Sánchez, G. Subías, J. García, and J. Blasco, Phys. Rev. B **69**, 184415 (2004).

[26] J. Farrell and G. A. Gehring, New J. Phys. **6**, 168 (2004).

[27] J. S. Zhou and J. B. Goodenough, Phys. Rev. B **77**, 172409 (2008).

[28] M. C. Sánchez, J. García, G. Subías, and J. Blasco, Phys. Rev. B **73**, 094416 (2006).

[29] I. S. Lyubutin, T. V. Dmitrieva, and A. S. Stepin, J. Exp. Theor. Phys. **88**, 590 (1999).

[30] I. A. Sergienko and E. Dagotto, Phys. Rev. B **73**, 094434 (2006).

[31] J. A. Rodgers, A. J. Williams, M. J. Martínez-Lope, J. A. Alonso, and J. P. Attfield, Chem. Mater. **20**, 4797 (2008).

[32] R. A. Cowley, Philos. Trans. R. Soc. London, Ser. B **290**, 583 (1980).